Supporting Information for

Heterometallic Trinuclear Oxo-centered Clusters as Single-Source Precursors for Synthesis of Stoichiometric Monodisperse Transition Metal Ferrite Nanocrystals

Karla R. Sanchez-Lievanos, Mehrin Tariq, William W. Brennessel, and Kathryn E. Knowles*

Department of Chemistry, University of Rochester, Rochester, NY 14627, United States

Table of Contents

Crystal Structures

Data collection

A crystal was placed onto a thin glass optical fiber or a nylon loop and mounted on a Rigaku XtaLab Synergy-S Dualflex diffractometer equipped with a HyPix-6000HE HPC area detector for data collection at 100.00(10) K (**2**, **3**, **4** and **5**) and K (**1**). A preliminary set of cell constants and an orientation matrix were calculated from a small sampling of reflections.[1] A short pre-experiment was run, from which an optimal data collection strategy was determined. The full data collection was carried out using a PhotonJet (Cu) X-ray source with frame times of 0.41 and 1.63 seconds for **1**, 0.91 and 3.63 seconds for **2**, of 0.14 and 0.57 seconds for **3**, 3.52 seconds (time frame) for **4**, 0.30 and 1.21 seconds for **5**, and a detector distance of 31.2 mm ((Mo) X-ray source and a detector distance of 34.0 mm for **4**). Series of frames were 0.50º steps in ω at different 2θ, κ, and ϕ settings. After the intensity data were corrected for absorption, the final cell constants were calculated from the xyz centroids of several strong reflections from the actual data collection after integration. See Table 1 for additional crystal and refinement information.

Structure solution and refinement

The structure was solved using ShelXT[2] and refined using ShelXL.[3] The space group *C*2/*c* for **1**, **2**, **4** and **5**, and the space group *P*-1 for **3** were determined based on systematic absences and intensity statistics. Most or all non-hydrogen atoms were assigned from the solution. Full-matrix least squares / difference Fourier cycles were performed which located any remaining non-hydrogen atoms. All non-hydrogen atoms were refined with anisotropic displacement parameters. The positions of hydrogen atoms on the aquo ligands and those of cocrystallized water solvent molecule O20 were based on the difference Fourier map and then given riding models. For **1**, **2**, **4**, and **5**: Hydrogen atoms on disordered cocrystallized water solvent molecules O17, O18, and O19 were unable to located in the difference Fourier map; they were not assigned but were included in the molecular formula. For **3**: Hydrogen atoms on aquo ligands O1 and O3 were found from the difference Fourier map and refined freely. Due to disorder (see below), the remaining O-H hydrogen atoms were placed in positions reasonable for hydrogen bonding and then given riding models. All other (methyl) hydrogen atoms from the cocrystallized acetone molecules were placed in ideal positions and refined as riding atoms with relative isotropic displacement parameters. The final full matrix least squares refinement converged to *R*1 and *wR*2 values that can be found on Table S1.

Structure description

The structures are the ones suggested. Isomorphous structures **1**, **2**, **4**, and **5** contain 3.5 co-crystallized water solvent molecules per cluster. Two of the three water molecules are modeled as disordered over general positions and the remaining half-molecule is modeled as disordered over a crystallographic two-fold axis. Hydrogen atoms were not placed on the disordered water

molecules, but included in the molecular formula. The cluster of structure **3** co-crystallized with one water and four acetone solvent molecules, all in general positions.

Two metal sites were modeled as a disorder of Fe and M: (**2**) Fe1:Co1, 0.91:0.09, Fe2:Co2, 0.49:0.51, Fe3:Co3, 0.60:0.40, (**3**) Fe1:Ni1, 0.92:0.08, Fe2:Ni2, 0.78:0.22, Fe3:Ni3, 0.30:0.70, (**4**) Fe1:Cu1, 0.91:0.09, Fe2:Cu2, 0.60:0.40, Fe3:Cu3, 0.50:0.50, and (**5**) Fe2:Zn2, 0.51:0.49 and Fe3:Zn3, 0.49:0.51. The metal ratio between the two sites was constrained to 2:1. The vertex labeled Fe1 in all bimetallic structures is modeled as entirely Fe(III) (**5**) or a site disorder of Fe(III)/M(II) for which Fe(III) refined to greater than 90 % based on the experimental data (**2**, **3**, **4**). The other two disordered metal sites refined to occupancies representing a more even mixture of the two oxidation states. And while the site labeled Fe1 could likely have been modeled as just Fe(III) in all the bimetallic structures (as it was in **5**), there was no crystallographic rationale why all three metal sites could not have had occupancy contributions from M(II). Therefore, all three metal centers in **2**, **3**, **4** and two metal centers in **5** were refined as site disorders of Fe(III)/M(II). Due to resolution limitations, the positional and anisotropic displacement parameters, respectively, at each metal site were constrained to be identical between the two element types. Thus the metal positions likely represent a weighted average of the individual positions based on element type. For example, in **2** the distance between μ_3-oxo atom (O16) and sites Fe1/Co1, Fe2/Co2, and Fe3/Co3 are 1.874(2), 1.926(2), and 1.931(2) Å, respectively, for which the obvious shorter bond length is due to the large contribution (91 %) of Fe(III) at site Fe1, relative to the more even mixture between Fe(III) and Co(II) in the other two sites. Because one metal site in each cluster is entirely or predominantly Fe(III), the metal centers form an approximate isosceles triangle, a result that is in agreement with the lowering of its symmetry from the ideal C_3 local symmetry of the trinuclear trivalent carboxylated clusters (See Fig. S17). CF_3 groups were modeled as disordered over two positions each (see cif files). Cocrystallized water solvent molecules O17, O18, and O19 were modeled as disordered over two positions each (see cif files). Structure manipulation and figure generation were performed using Olex2.[4] Unless noted otherwise all structural diagrams containing anisotropic displacement ellipsoids are drawn at the 50 % probability level.

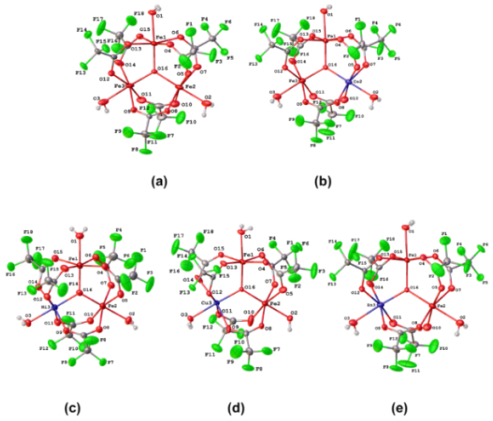

Figure S1. Crystal Structures of **(a) 1**, **(b) 2**, **(c) 3**, **(d) 4** and **(e) 5**, shown with 50% probability ellipsoids.

Table S1. Crystal data and structure refinement for **1**, **2**, **3**, **4** and **5**

Properties	1	2	3	4	5
CCDC Deposition Number	**1996873**	**1996870**	**1996871**	**1996872**	**1996869**
Identification code	KNOKS16	KNOKS11	KNOKS17	KN0KS12MO	KNOKS14
Empirical formula	$C_{12}H_{13}F_{18}Fe_3O_{19.50}$	$C_{12}H_{13}CoF_{18}Fe_2O_{19.50}$	$C_{24}H_{32}F_{18}Fe_2NiO_{21}$	$C_{12}H_{13}CuF_{18}Fe_2O_{19.50}$	$C_{12}H_{13}F_{18}Fe_2ZnO_{19.50}$
Formula weight	978.77	981.85	1168.90	986.46	988.29
Temperature (K)	99.97(10)	100.00(10)	100.00(10)	100.00(10)	100.00(10)
Wavelength (Å)	1.54184	1.54184	1.54184	0.71073	1.54184
Crystal system	Monoclinic	Monoclinic	Triclinic	Monoclinic	Monoclinic
Space group	*C*2/*c*	*C*2/*c*	*P*-1	*C*2/*c*	*C*2/*c*
Unit cell dimensions	*a* = 33.7504(3) Å α = 90°	*a* = 33.6911(3) Å α = 90°	*a* = 10.56550(10) Å α = 92.6340(10)°	*a* = 33.6407(8) Å α = 90°	*a* = 33.6920(4) Å α = 90°
	b = 10.71550(10) Å β = 92.8530(10)°	*b* = 10.7211(2) Å β = 92.6060(10)°	*b* = 11.5802(2) Å β = 97.2410(10)°	*b* = 10.6483(3) Å β = 93.306(2)°	*b* = 10.70450(10) Å β = 92.6740(10)°
	c = 16.4299(2) Å γ = 90°	*c* = 16.4167(2) Å γ = 90°	*c* = 19.90320(10) Å γ = 111.9130(10)°	*c* = 16.5280(4) Å γ = 90°	*c* = 16.4568(2) Å γ = 90°
Volume ($Å^3$)	5934.55(11)	5923.67(14)	2229.74(5)	5910.7(2)	5928.78(12)
Z	8	8	2	8	8
Calculated Density (Mg/m^3)	2.191	2.202	1.741	2.217	2.214
Absorption coefficient (mm^{-1})	13.478	13.962	7.022	1.877	10.561
F(000)	3848	3856	1172	3872	3880
Crystal color, morphology	red, block	red-orange, plate	orange, plate	red-orange, block	orange-red, plate
Crystal size (mm^3)	0.206 x 0.192 x 0.109	0.302 x 0.169 x 0.084	0.399 x 0.078 x 0.054	0.337 x 0.165 x 0.153	0.263 x 0.197 x 0.181
Theta range for data collection (°)	2.622 to 77.792	2.626 to 77.885	4.136 to 78.059	2.469 to 33.171	2.626 to 77.758
Index ranges	$-42 \le h \le 42$, $-13 \le k \le 9$, $-20 \le l \le 20$	$-42 \le h \le 42$, $-13 \le k \le 9$, $-20 \le l \le 20$	$-13 \le h \le 13$, $-14 \le k \le 13$, $-24 \le l \le 25$	$-46 \le h \le 49$, $-15 \le k \le 13$, $-24 \le l \le 24$	$-42 \le h \le 41$, $-13 \le k \le 13$, $-16 \le l \le 20$
Reflections collected	26694	27273	37017	32063	26971
Independent reflections	6218 [*R*(int) = 0.0504]	6194 [*R*(int) = 0.0656]	9354 [*R*(int) = 0.0731]	9615 [*R*(int) = 0.0254]	6185 [*R*(int) = 0.0500]
Observed reflections	5776	5847	8318	8563	5851
Completeness to theta = 74.504°	99.3%	99.4%	99.7%	99.8%	99.2%
Absorption correction	Multi-scan	Multi-scan	Multi-scan	Multi-scan	Multi-scan
Max. and min. transmission	1.00000 and 0.46891	1.00000 and 0.15910	1.00000 and 0.69858	1.00000 and 0.69082	1.00000 and 0.29311
Refinement method	Full-matrix least-squares on F^2	Full-matrix least-squares on F^2	Full-matrix least-squares on F^2	Full-matrix least-squares on F^2	Full-matrix least-squares on F^2
Data / restraints / parameters	6218 / 198 / 585	6194 / 152 / 560	9354 / 280 / 745	9615 / 519 / 638	6185 / 225 / 562
Goodness-of-fit on F^2	1.079	1.051	1.053	1.150	1.019
Final *R* indices [*I*>2sigma(*I*)]	*R*1 = 0.0477, *wR*2 = 0.1325	*R*1 = 0.0550, *wR*2 = 0.1498	*R*1 = 0.0522, *wR*2 = 0.1403	*R*1 = 0.0448, *wR*2 = 0.0934	*R*1 = 0.0511, *wR*2 = 0.1353
R indices (all data)	*R*1 = 0.0503, *wR*2 = 0.1347	*R*1 = 0.0567, *wR*2 = 0.1517	*R*1 = 0.0571, *wR*2 = 0.14	*R*1 = 0.0516, *wR*2 = 0.0957	*R*1 = 0.0528, *wR*2 = 0.1371
Largest diff. peak and hole ($e.Å^{-3}$)	0.761 and -1.179	0.955 and -1.261	0.614 and -1.391	0.995 and -1.012	1.045 and -0.998

Table S2. Selected distances and angles in clusters **1-5**

	1	**2**	**3**	**4**	**5**
Distances (Å)					
Fe(1,2)-O(16)$_{avg}$	1.900	1.900	1.885	1.903	1.906
M-O(16)	1.948	1.931	1.959	1.923	1.943
Angles (°)					
Fe(1)-O(16)-Fe(2)	121.110	121.186	121.275	121.274	121.172
Fe(1,2)-O(16)-M$_{avg}$	119.445	119.4065	119.361	119.578	119.413

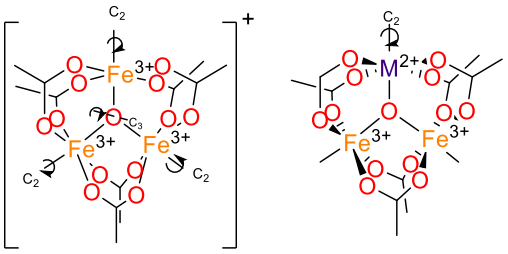

Figure S2. Site symmetry differences between trivalent and mixed-valence mixed-metal oxo-centered carboxylated clusters as well as the space group where they tend to crystallize in.

Table S3. Summary of Absorption Data for Clusters **1-5**

Cluster	**Single source precursor molecular formula**	**λ_{max}[nm] (ε[$M^{-1}cm^{-1}$])**
1	$Fe_3(\mu_3\text{-}O)(\mu_2\text{-}OOCCF_3)_6(OH_2)_3\cdot 3.5(H_2O)$	232(11050), 310(4390), 357(4266), 525(277)
2	$CoFe_2(\mu_3\text{-}O)(\mu_2\text{-}OOCCF_3)_6(OH_2)_3\cdot 3.5(H_2O)$	232(9564), 305(3583), 340(3302), 447(528), 516 (140)
3	$NiFe_2(\mu_3\text{-}O)(\mu_2\text{-}OOCCF_3)_6(OH_2)_3\cdot 4C(O)Me_2\cdot H_2O$	237(5708), 303(2390), 350(2085), 563(67), 727(22)
4	$CuFe_2(\mu_3\text{-}O)(\mu_2\text{-}OOCCF_3)_6(OH_2)_3\cdot 3.5(H_2O)$	242(8465), 304(4175), 329(3487), 453(344), 760 (63)
5	$ZnFe_2(\mu_3\text{-}O)(\mu_2\text{-}OOCCF_3)_6(OH_2)_3\cdot 3.5(H_2O)$	236(9119), 303(4011), 343(3643), 465(342), 537(142)

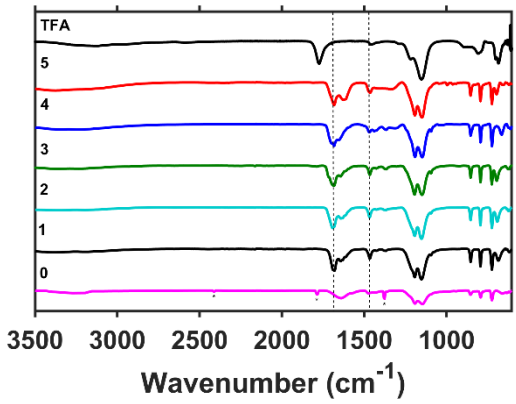

Figure S3. FTIR spectra of the clusters **1-5** and free trifluoroacetic acid (TFA). The dotted lines indicate the symmetric and asymmetric OCO^- stretching modes that correspond to the bridging bidentate binding mode of the carboxylate ligand to the triangular metal oxo-centered core. Compound **0** corresponds to the all-iron(III) cluster, the asterisks indicate the characteristic bands of NO_3^- since the counterion of this cluster is NO_3^-.

The two intense peaks > 1600 cm^{-1} are both assigned to the asymmetric OCO^- stretch (see Table S4 below). This band splits slightly due to the reduction of site symmetry upon replacing an Fe(III) center with an M(II) center, which lifts the degeneracy of the asymmetric OCO stretch in the mixed-valent clusters compared to the all-Fe(III) cluster. The band at 1775-1780 cm^{-1} in the spectrum of free trifluoroacetic acid, which is assigned to $\nu_{C=O}$, is replaced in the spectra of the clusters by two intense bands, $\nu_{as(OCO)} \approx$ 1630-1694 cm^{-1} and $\nu_{s(OCO)} \approx$ 1470-1475 cm^{-1}. The magnitude of the separation $\Delta\nu = \nu_{as} - \nu_s$ is directly linked to the mode of coordination of the carboxylate ions. The $\Delta\nu$ values of ~160-220 cm^{-1} observed here suggest a bridging bidentate bonding mode.

Table S4. FT-IR Data Analysis for clusters **1-5** (cm^{-1})[6,7]

Cluster	ν $(MFe_2O)_{as}$	δ (OCO)	δ (CCO_2)	δ (CF_3)	ν (CC)	ν (CF_3)	ν (FCF_2)	δ (COH)	N $(COO^-)_s$	ν $(COO^-)_{as}$	ν $(COO^-)_{as}$
1	623	686.7	725.2	794.7	854.5	1152	1196	1366	1468	1636	1688
2	628	692.4	725.2	794.7	854.5	1153	1194	1369	1472	1630	1694
3	629	696.3	725.2	794.7	854.5	1150	1196	1368	1473	1649	1684
4	630	665.4	725.2	794.7	854.5	1150	1192	1371	1474	1650	1684
5	640	696.3	725.2	794.7	854.5	1150	1196	1346	1474	1649	1682

Cluster	$\nu(CH_3)$	$\nu_{as}(OCO^-)$	$\nu_{sym}(OCO^-)$	$\delta(CH_3)$	$\rho_{oop}(CH_3)$	ν(C-C)	Fe_3O
1a	2961	1568, 1560	1422	1360	1038	909	658
1b	w, b	1581	1420	1346	1034	950	632

Both **1a** and **1b** show additional peaks that correspond only to free acetate or pivalate anions (from unreacted acid) as an impurity; however, no extra peaks from chlorine or nitrate anions can be observed. Unreacted acid was further removed from the bulk by applying dynamic vacuum for 24 h before the solid was used in the solvothermal reaction. w, b = weak and broad.

Figure S4. Representative solubility test on cluster **3** dissolved in **(a)** acetonitrile, **(b)** acetone and **(c)** pyridine.

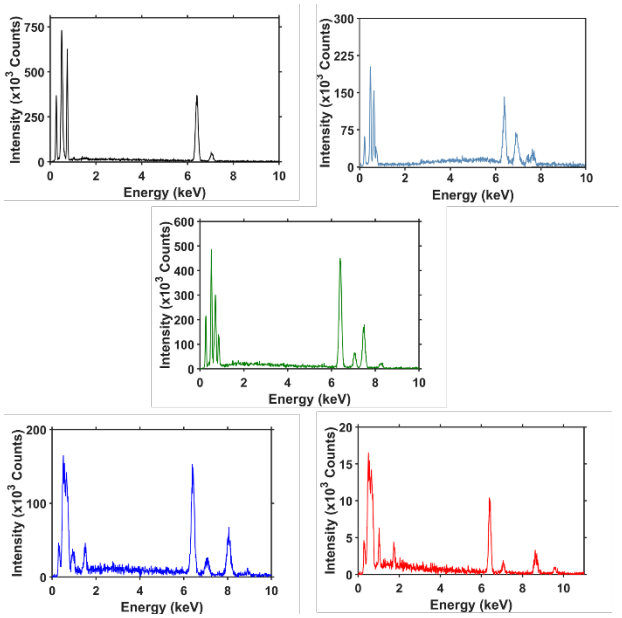

Figure S5. EDS Spectra of clusters **1-5** depicted in the colors assigned to each cluster through the manuscript.

Table S5. Percent composition of M and Fe in clusters 1-**5** measured by EDS.

	1		**2**		**3**		**4**		**5**	
Element	Atomic %	keV	Atomic %	keV	Atomic %	keV	Atomic %	keV	Atomic %	keV
Fe K	100	6.39	66.71	6.39	66.59	6.40	67.36	6.39	65.83	6.40
M K	-	-	33.29	6.93	33.41	7.47	32.64	8.04	34.17	8.63

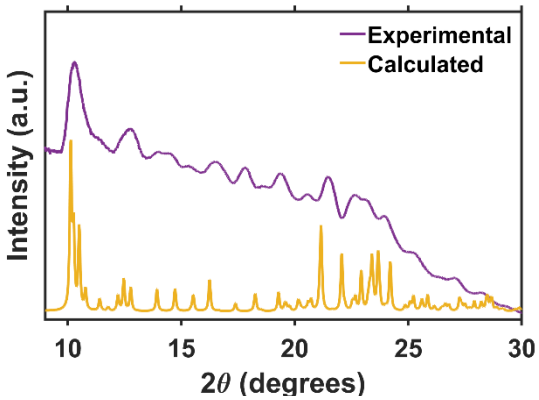

Figure S6. p-XRD diffractogram of pulverized **2** against the calculated pattern from Mercury showing the purity of the cluster as a bulk.

Reproducibility test

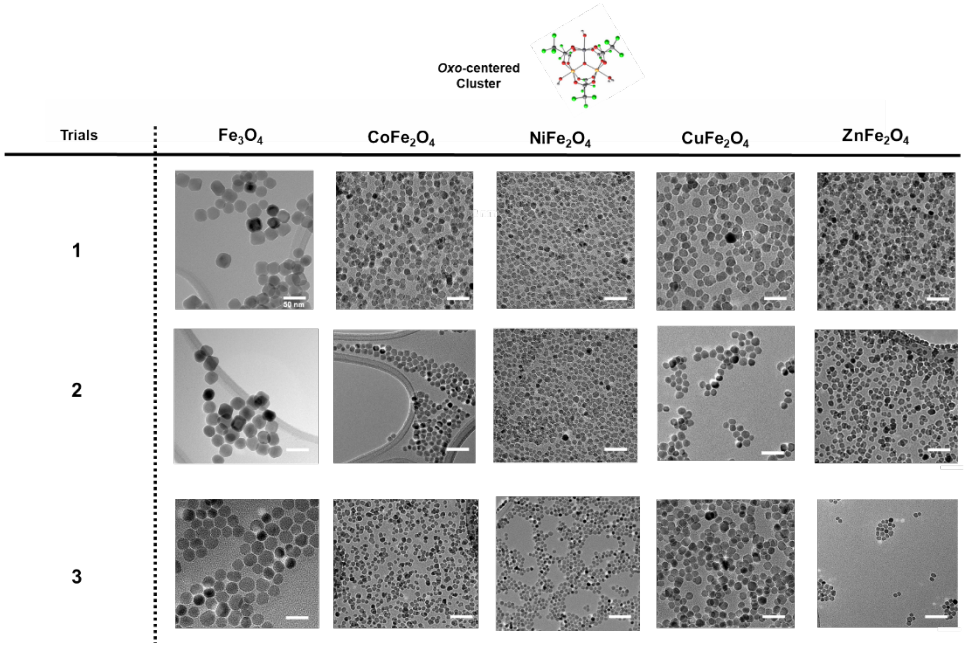

Figure S7. Representative TEM images from three different trials of each nanocrystal reaction using cluster precursors.

Table S6. Statistical Analysis of the Sizes of MFe_2O_4 Nanocrystals Synthesized from Clusters **1**-**5** [nm]. PDI in parenthesis.

Metal Ferrite	1	2	3	Average Diameter	Weighted STD	Overall PDI
Fe_3O_4	**29.8** ± 1.7 (0.06)	**30.2** ± 1.9 (0.06)	**32.7** ± 2.5 (0.08)	**30.9**	1.19	0.04
$CoFe_2O_4$	**10.3** ± 0.8 (0.07)	**12.3** ± 1.2 (0.10)	**9.8** ± 1.3 (0.13)	**10.8**	0.65	0.06
$NiFe_2O_4$	**7.9** ± 1.1 (0.14)	**8.4** ± 1.3 (0.15)	**7.2** ± 1.0 (0.14)	**7.8**	0.66	0.08
$CuFe_2O_4$	**16** ± 1.3 (0.08)	**15.2** ± 1.2 (0.08)	**16.3** ± 1.4 (0.09)	**15.8**	0.75	0.05
$ZnFe_2O_4$	**10.4** ± 1.4 (0.13)	**9.5** ± 1.3 (0.14)	**11.2** ± 1.6 (0.14)	**10.4**	0.83	0.08

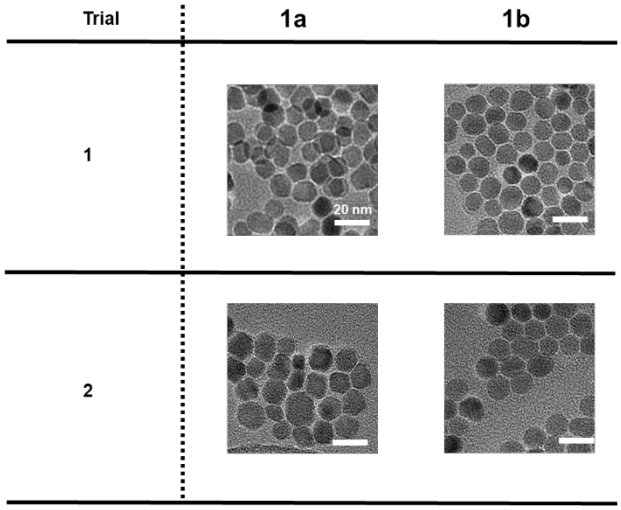

Figure S8. Representative TEM images from two different trials of Fe_3O_4 nanocrystal reaction using cluster precursors **1a** and **1b**.

Table S7. Statistical Analysis of the Sizes of Fe_3O_4 Nanocrystals Synthesized from Clusters **1a** and **1b**.[a]

Cluster	1[b]	2[b]	Average Diameter	Weighted standard dev.	Overall PDI
1a	**16.4** ± 1.2 (0.07)	**17.6** ± 2.2 (0.12)	**17.0**	1.25	0.07
1b	**14.3** ± 0.7 (0.05)	**16.5** ± 1.3 (0.08)	**15.4**	0.74	0.05

[a]All diameters and standard deviation values are provided in units of nanometers. [b]PDI values are given in parentheses.

The weighted average standard deviation[5] was calculated from the equation S1.

$$\langle\sigma\rangle = \frac{\sqrt{\sigma_1^2 N_1^2 + \sigma_2^2 N_2^2}}{N_1 + N_2 + N_3} \quad \text{(S1)}$$

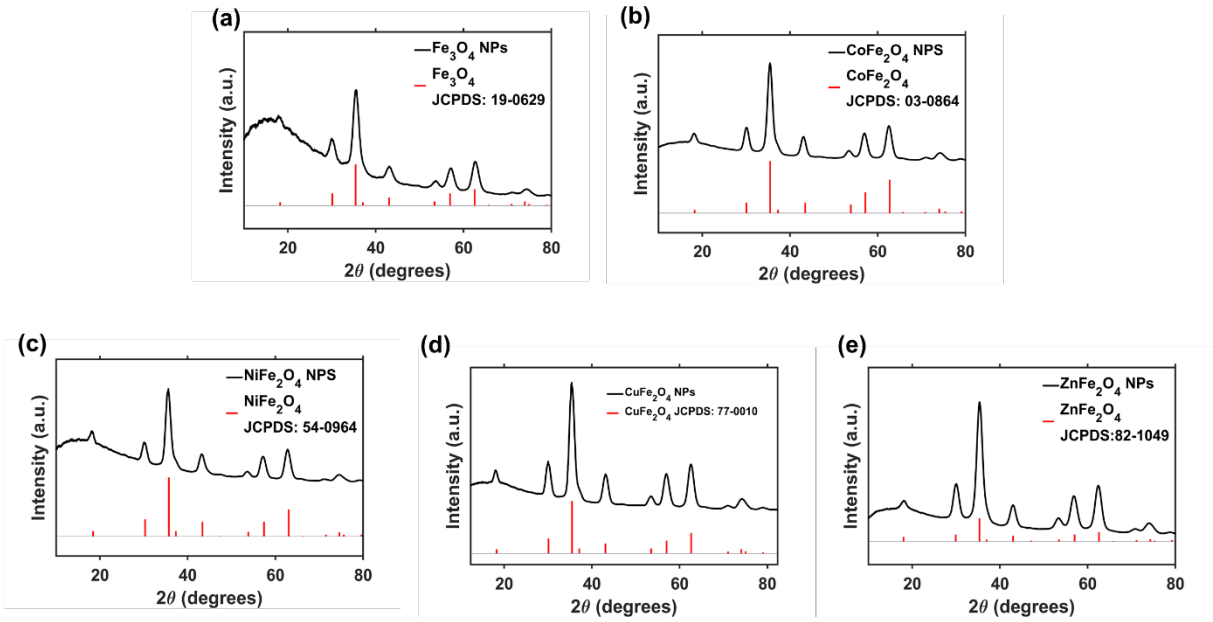

Figure S9. XRD Pattern matching JCPDS reference data for all the synthesized metal ferrite nanoparticles

Conversion of the XRD pattern taken using Molybdenum Kα to Copper Kα

The data needs to be converted into q space, namely the momentum transfer:

$$Q = \frac{(4\pi \sin(\theta))}{\lambda}$$

θ: Diffraction angle (°)

λ: X-ray wavelength (Å)

Since:

$$\lambda = hc/E$$

h: Planck's constant

c: speed of light

E: X-ray energy (keV)

E1: 1.7445×10^4 eV (Mo), E2: 8.0432×10^3 eV (Cu).

Now the theta angles measured can be interconverted to the ones expected for copper.

$$\lambda \cong 12398.5/E$$

$$Q(\text{Å}^{-1}) = \left(\frac{4\pi}{12.3985}\right) * E1 * sin(\theta_1) = \left(\frac{4\pi}{12.3985}\right) * E2 * sin(\theta_2)$$

Therefore:

$$\theta_2 = (arcsin\left(\frac{E_1}{E_2} \sin(\theta_1)\right)$$

This conversion calculation is only valid for crystal phase peak identification.

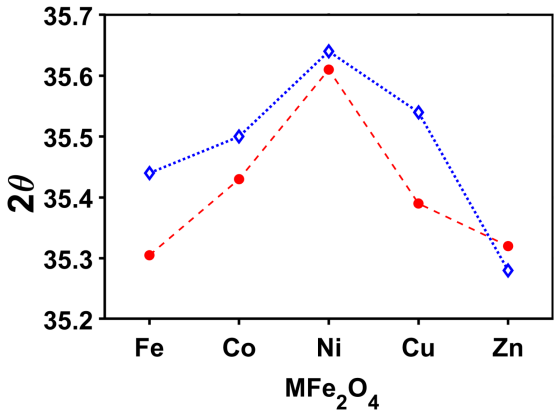

Figure S10. Plot of the 2θ values corresponding to diffraction from the {311} plane for MFe_2O_4 where M = Fe, Co, Ni, Cu, Zn. The solid red circles plot data extracted from the diffractograms shown in Figure 4 and the open blue diamonds plot data obtained from previously reported single crystal structures.[8-12]

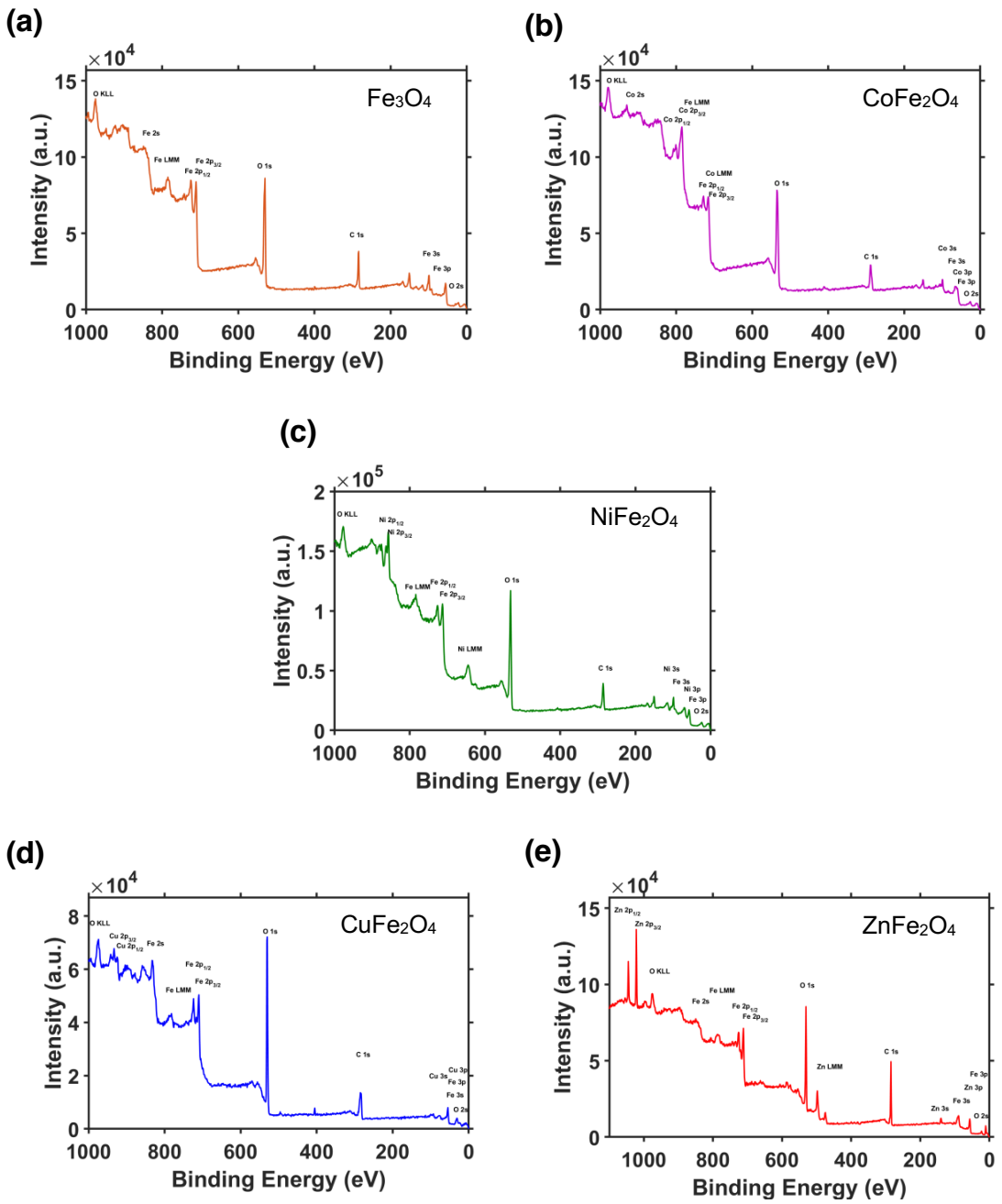

Figure S11. (**a-e**) X-ray photoelectron survey spectra of the MFe_2O_4 nanocrystals synthesized from clusters **1-5**. For each sample, the scan indicates the presence of M, Fe, O, and C (from surface ligands).

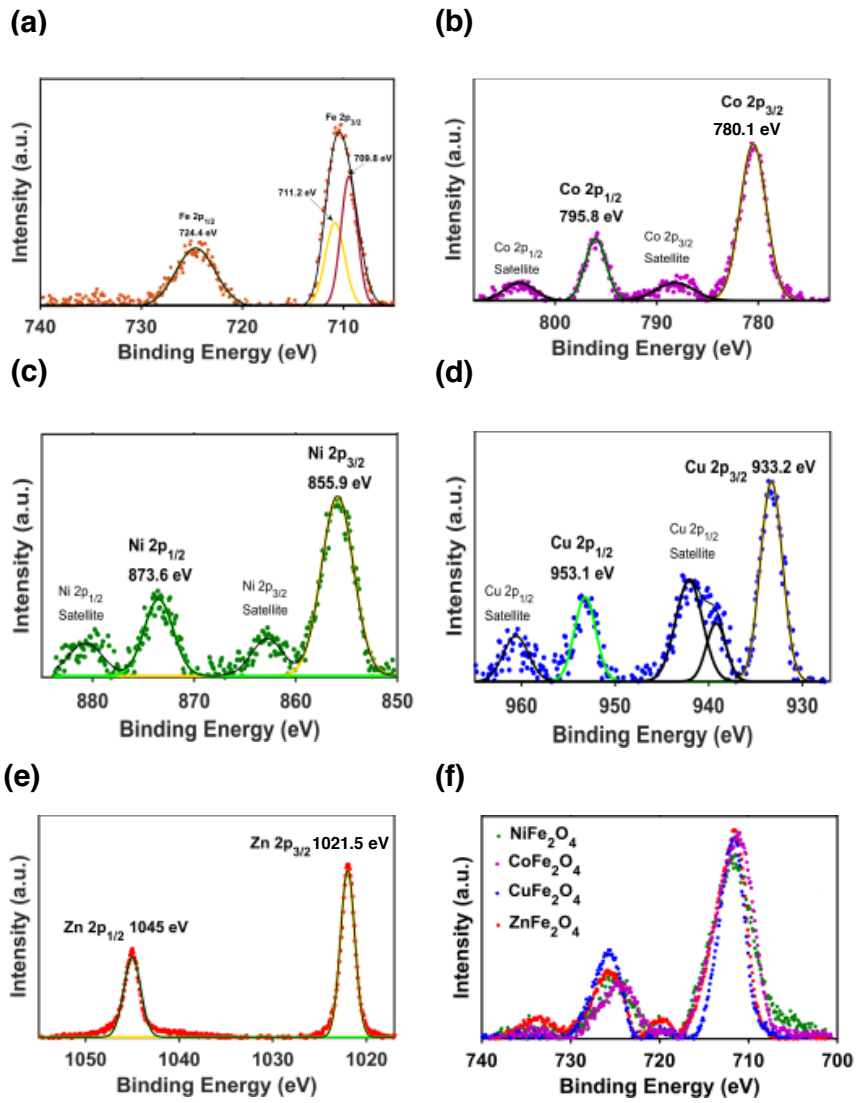

Figure S12. X-ray photoelectron spectra of the **(a)** Fe 2p, **(b)** Co 2p, **(c)** Ni 2p, **(d)** Cu 2p and **(e)** Zn 2p regions for the corresponding MFe_2O_4 nanocrystals. Experimental data is plotted with colored circles and the solid lines represent Gaussian fits of the observed peaks. Each spectrum contains only one set of 2p peaks, which is consistent with the presence of only one oxidation state. The Co, Ni, and Cu spectra each contain satellite peaks characteristic of an open-shell configuration. The Zn 2p spectrum does not contain any satellite peaks, which is consistent with the closed-shell electronic configuration of Zn^{2+}. **(f)** XPS of the Fe 2p region for MFe_2O_4 nanocrystals (M = Co, Ni, Cu, Zn).

Table S8. EDS Data Collected from MFe_2O_4 nanocrystals (**1-N** – **5-N**) synthesized from clusters **1-5**

Element	Line s.	Atomic (%)	Normalized Mass (%)
M:			
Co (**2-N**)		13.7	24.5
Ni (**3-N**)	K-Serie	14.9	25.5
Cu (**4-N**)		14.3	26.5
Zn (**5-N**)		12.4	25.2
Iron			
1-N		39.1	69.1
2-N		27.8	47.1
3-N	K-Serie	30.1	48.9
4-N		28.9	47.0
5-N		25.0	43.5
Oxygen			
1-N		60.9	30.8
2-N		58.5	28.4
3-N	K-Serie	55.0	25.6
4-N		56.8	26.5
5-N		62.6	31.2

Table S9. M:Fe:O ratio determined from EDS measurements of MFe_2O_4 nanocrystals

Ferrospinel	EDS Ratio (M:Fe:O)
Fe_3O_4	**1:1.60***
$CoFe_2O_4$	**1:2.03:4.30***
$NiFe_2O_4$	**1:2.02:4.00**
$CuFe_2O_4$	**1:2.02:4.00**
$ZnFe_2O_4$	**1:2.02:5.00***

The EDS Ratio highlighted with an asterisk (*) symbolizes the excess of oxygen due to the presence of some remaining ligands on the surface of the nanoparticles. This also agrees with the observable peak of Carbon K_α on the region around 0.27 and 0.3 eV, see Figure S7 below.

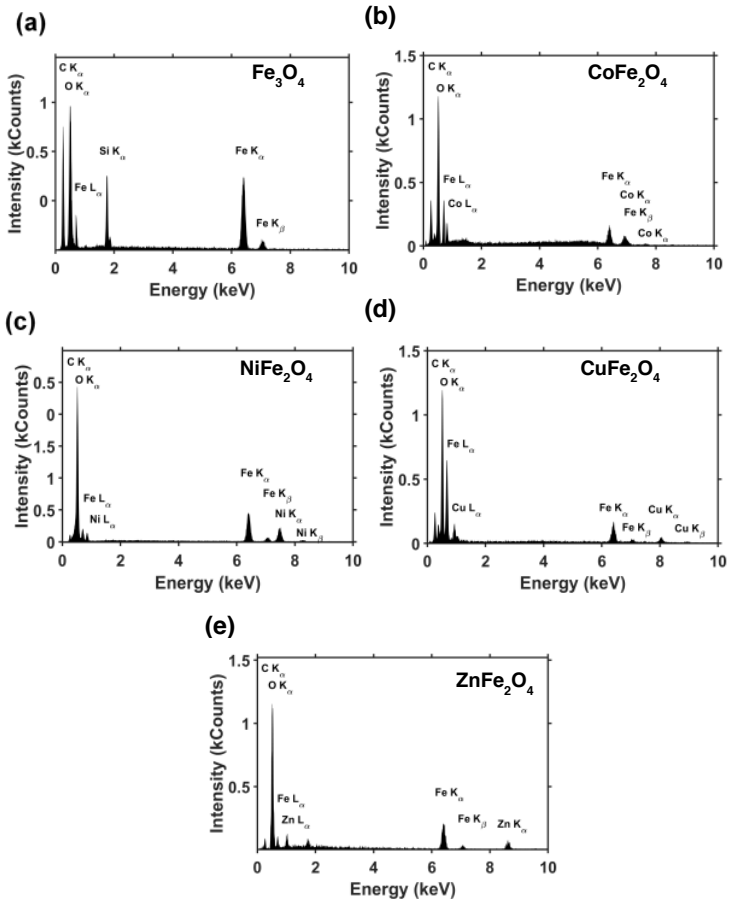

Figure S13. Energy dispersive X-ray spectra of MFe_2O_4 nanocrystals.

The MFe_2O triangular unit in the cluster is related structurally to one observed in the spinel crystal lattice. The triangular motif connectivity remains present in the spinel lattice, but there are some differences in the three-dimensional geometry. Specifically, in the spinel ferrite lattices the M-Fe-Fe-O dihedral angle (θ) [$20° < \theta < 40°$] is significantly larger than the one observed in the cluster structure, which is close to 0° (0.09° (**1**), 0.165° (**2**), 0.345° (**3**), 0.227° (**4**) and 0.334° (**5**)), and the angles between M-Fe-Fe in the spinel lattice are smaller than those observed in the cluster by ~10°. Moreover, the Fe-O-Fe angle in the metal ferrite lattice tends to present values around right angles, whereas in the clusters these angles are larger than 90°. However, the Fe-O-M angles for both structures are ~120°.

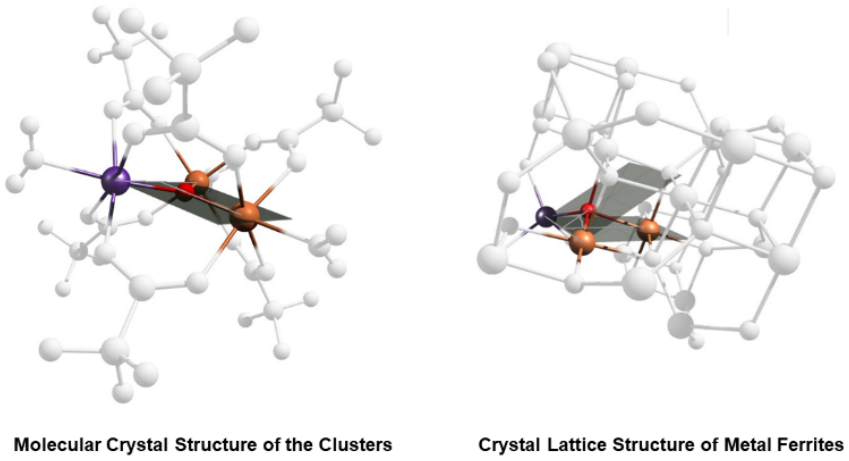

Figure S14. Three-dimensional visualization of the triangular scaffold of both the cluster and the metal ferrite lattice structures.

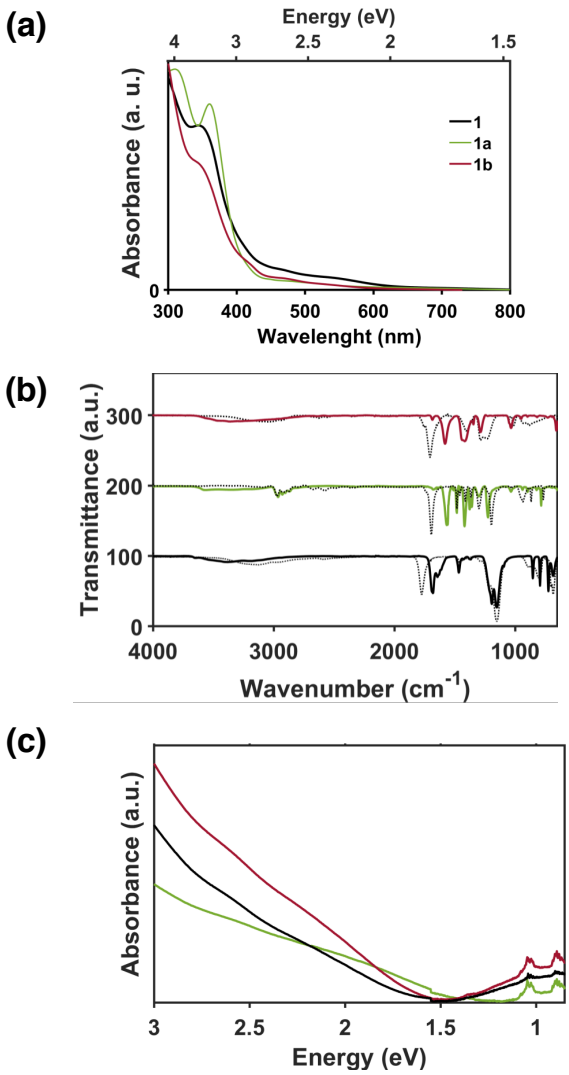

Figure S15. (**a**) UV-Vis Absorption Spectra of **1** (black), **1a** (green), and **1b** (red). (**b**) FT-IR Transmittance Spectra of **1**, **1a** and **1b** compared to the initial protonated carboxylic acid (doted lines) used as chelating ligand for the trimeric core structure. (**c**) UV-Vis absorption spectra of hexane dispersions of Fe_3O_4 nanocrystals synthesized from clusters **1**, **1a**, **1b** highlighting the features below 1.5 eV corresponding to the IVCT transition between Fe^{2+} and Fe^{3+} ions in octahedral sites ($^6A_1 \rightarrow {}^4T_1(G)$).

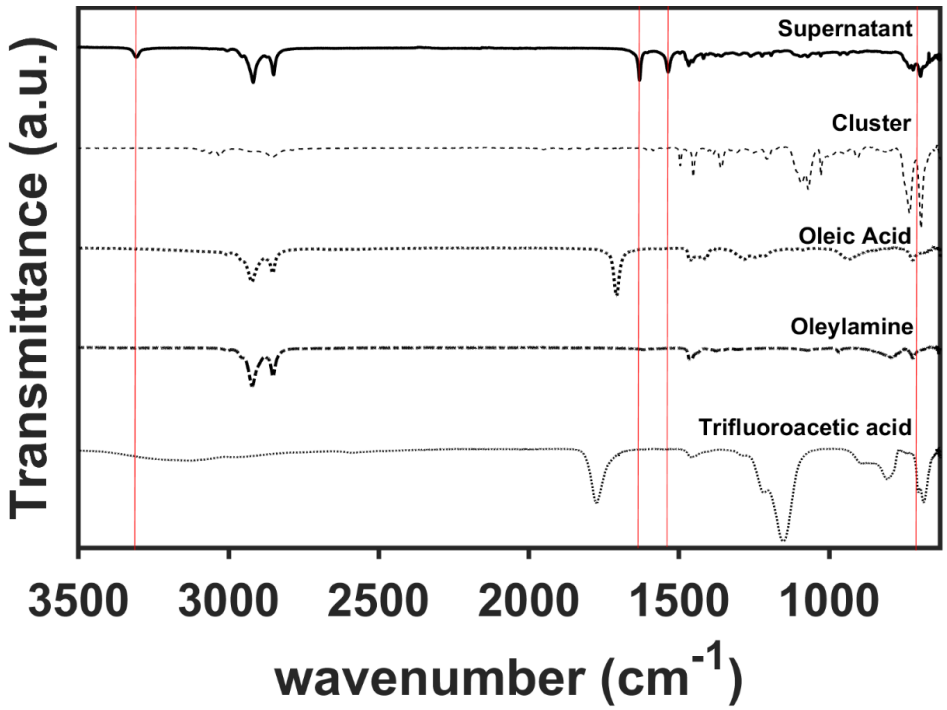

Figure S16. FT-IR contrasting the transmittance spectra of the input materials of the solvothermal reaction *versus* the resulting reaction supernatant. Bands at 3308, 1653, 1535 and 696 cm^{-1} (indicated by the vertical red lines) strongly indicate the presence of an amide, which supports the proposed mechanism in Scheme 2.

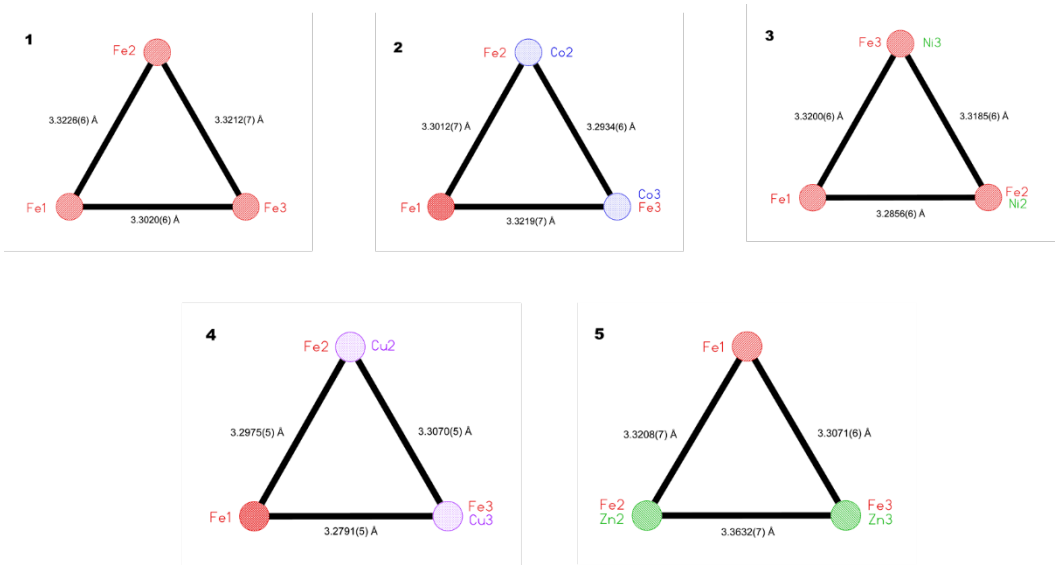

Figure S17. Representative edge distances within the triangular scaffold of clusters **1-5.**

References

1. *CrysAlisPro*, version 171.40.71a; Rigaku Corporation: Oxford, UK, 2020.
2. G. M. Sheldrick, *SHELXT*, version 2018/2; *Acta. Crystallogr. A*, 2015, ***71***, 3-8.

3. G. M. Sheldrick, *SHELXL*, version 2018/3; *Acta. Crystallogr. C,* 2015, ***71***, 3-8.
4. O. V. Dolomanov, L. J. Bourhis, R. J. Gildea, J. A. K. Howard and H. Puschmann, *Olex2*, version 1.2-ac3, *J. Appl. Cryst.* 2009, ***42***, 339-341.
5. J. R. Taylor, *An Introduction to Error Analysis: The Study of Uncertainties in Physical Measurements*; 2nd ed.; University Science Books: Sausalito, CA, 1997.
6. R. L. Redington and K. C. Lin, *Spectrochim. Acta A*, 1971, **27**, 2445-2460.
7. C. V. Berney, J. Amer. Chem. Soc., 1973, **95**, 708.
8. M. C. Blesa, U. Amador, E. Morán, N. Menéndez, J. D. Tornero and J. Rodríguez-Carvajal, *Solid State Ionics*, 1993, **63**, 429-436.
9. T. A. S. Ferreira, J. C. Waerenborgh, M. H. R. M. Mendonça, M. R. Nunes and F. M. Costa, *Solid State Sci*., 2003, **5**, 383-392.
10. M. E. Fleet, J. *Solid State Chem.*, 1986, **62**, 75-82.
11. P. F. P. Teh, S. S.; Kim, C.; Chen, C.-M.; Chuang, C.-H.; Sharma, Y.; Cabana, J.; Madhavi, S. , *J. Phys. Chem. C.*, 2013, **117**, 24213-24223.
12. E. J. W. Verwey and E. L. Heilmann, *J. Chem. Phys.*, 1947, **15**, 174-180.